



Microarchitected 3D printed polylactic acid (PLA) nanocomposite scaffolds for biomedical applications

Fahad Alam^a, Vishnu Raj Shukla^b, K.M. Varadarajan^{c,d}, S. Kumar^{a,*}

^a Department of Mechanical Engineering, Khalifa University, Masdar Campus, Masdar City, Abu Dhabi, United Arab Emirates

^b Biomaterial Processing and Characterization Laboratory, Department of Materials Science and Engineering, Indian Institute of Technology Kanpur, Kanpur, 208016, UP, India

^c Department of Orthopaedic Surgery, Harris Orthopaedics Laboratory, Massachusetts General Hospital, 55 Fruit St, Boston, USA

^d Department of Orthopaedic Surgery, Harvard Medical School, A-111, 25 Shattuck Street, Boston, USA

ARTICLE INFO

Keywords:

Anti-bacterial
Scaffolds
Metal/alloy filled PLA
3D printing
Surface treatment

ABSTRACT

Anti-bacterial scaffolds made of copper, bronze and silver particles filled PLA nanocomposites were realized via fused filament fabrication (FFF), additive manufacturing. The thermal, mechanical and biological characteristics including bioactivity and bactericidal properties of the scaffolds were evaluated. The incorporation of bronze particles into the neat PLA increases the elastic modulus up to 10% and 27% for samples printed in 0° and 90° configurations respectively. The stiffness increases, up to 103% for silver filled PLA nanocomposite scaffolds. The surface of scaffolds was treated with acetic acid to create a thin porous network. Significant increase (~20–25%) in the anti-bacterial properties and bioactivity (~18–100%) is attributed to the synergetic effect of reinforcement of metallic/metallic alloy particles and acid treatment. The results indicate that PLA nanocomposites could be a potential candidate for bone scaffold applications.

1. Introduction

Polylactic acid (PLA) has been explored for biomedical scaffold applications because of its biocompatibility, biodegradability, non-toxic, non-immunogenic and non-inflammatory properties towards the human body. PLA is produced from the starch obtained from biological sources such as corn, sugar beets, sugar cane, wheat, etc. The starch is processed either by fermentation or other chemical processes (Shirai et al., 2018) to obtain PLA. Owing to its biocompatibility, biodegradability and bioresorbability, PLA is a suitable candidate for temporary scaffold implants (Paolini et al., 2018; Saito et al., 2001; Wang et al., 2017b) and is extensively being explored for tissue engineering applications. The other polymeric materials used for temporary scaffold applications are natural fibers based polymer composites such as chitosan, silk fiber and collagen (Almeida et al., 2014; Balagangadharan et al., 2017; Cavinin et al., 2018; Dong et al., 2017; Sharif et al., 2018). Among these polymer composite scaffolds chitosan-based scaffolds with porous structure have been studied extensively (Balagangadharan et al., 2017; Dhivya et al., 2015; Levengood and Zhang, 2014; Menon et al., 2018; Preethi Soundarya et al., 2018; Saravanan et al., 2017; Sivashankari and Prabakaran, 2016). To introduce functional properties to PLA,

researchers incorporated fillers such as hydroxyapatite to improve bioactivity (Persson et al., 2014; Tanodekaew et al., 2013), allotropes of carbon (CNT, CNF and GNP) to introduce piezoresistivity (Alam et al., 2019a; Bayer, 2017; Cataldi et al., 2018; Gupta et al., 2018; Kumar et al., 2019; Patole et al., 2019; Reddy et al., 2018) and magnetic particles for magnetic resonance imaging (MRI) applications (Xu et al., 2011). However, the anti-bacterial activity with the addition of different filler materials is yet to be explored. PLA nanocomposites filled with micro-fillers such as copper, bronze and silver filled PLA may have adequate anti-bacterial properties because of the bactericidal nature of copper, bronze and silver. Several routes exist to prepare metal/metal alloy filled PLA composites such as solvent casting (Feng et al., 2018; Sousa et al., 2019), molding (e.g. compression and injection) (Harris and Lee, 2008; Nakagaito et al., 2009; Volpe et al., 2018), *in situ* polymerization (Li et al., 2013) and additive manufacturing (Arif et al., 2018; Dugbenoo et al., 2018; Ertane et al., 2018; Kumar et al., 2016; Li et al., 2018; Rajkumar and Shanmugam, 2018; Ubaid et al., 2018). Among the aforementioned techniques, additive manufacturing (3D printing) is one of the most suitable techniques for the fabrication of scaffolds because it enables fabrication of complex geometry with controlled porosity—a very important consideration for tissue engineering scaffold applications

* Corresponding author.

E-mail address: s.kumar@eng.oxon.org (S. Kumar).

<https://doi.org/10.1016/j.jmbbm.2019.103576>

Received 29 August 2019; Received in revised form 1 October 2019; Accepted 29 November 2019

Available online 3 December 2019

1751-6161/© 2019 The Authors.

Published by Elsevier Ltd.

This is an open access article under the CC BY-NC-ND license

(<http://creativecommons.org/licenses/by-nc-nd/4.0/>).

(Wang et al., 2017a) for appropriate cell penetration, fluid flow and waste removal.

Fused filament fabrication (FFF) (also known as fused deposition modeling, FDM), is mostly used for processing thermoplastic polymers with complex architectures (Gnanasekaran et al., 2017; Kumar et al., 2016; Singh et al., 2014; Upadhyay et al., 2017; Xiaoyong et al., 2017). In FFF, the filament is fed through a pre-heated nozzle and melt extruded to deposit the melt as per the computer-aided design (CAD) model. The layer-by-layer deposition takes place to build a complete 3D structure by lowering the print bed in Z direction while moving the print head along X and Y axes. The print bed is lowered after each layer is deposited and next layer is deposited on top of pre-deposited layer (Huang et al., 2018; Jammalamadaka and Tappa, 2018; Wang et al., 2017a). Because of the positive glass transition temperature and high melt stability, PLA is easily processable via FFF-3D printing (Ligon et al., 2017; Salentijn et al., 2017).

In the current study, the scaffolds of PLA and its nanocomposites filled with metal/metal alloy particles were fabricated using FFF additive manufacturing. Scaffolds with interconnected porous network having 50% porosity were designed and 3D printed. The physical, thermal and microstructural characterization of 3D printed scaffolds were performed and analyzed. To evaluate mechanical properties, compression test was performed on all the 3D printed scaffolds. Furthermore, tensile test was performed on 3D printed dogbone samples with 100% infill density considering two different printing directions (0° and 90°). *In vitro* bioactivity assessment was performed by immersion test in simulated body fluid (SBF) and growth of apatite layer was analyzed using SEM and XRD. Furthermore the anti-bacterial activity of the scaffolds was evaluated with gram-negative, *Escherichia coli* (*E. coli*) and gram positive, *Staphylococcus aureus* (*S. aureus*) bacterial cells.

2. Materials and methods

2.1. Materials

Filament of neat PLA of was obtained from LeapFrog 3D Printers (Alphen aan den Rijn, The Netherlands) and filaments of metal/metal alloy filled PLA were purchased from Formfutura, Netherland. The details of filaments, amount of filler, type of filler materials and their assigned sample IDs are given in Table 1. SBF used for bioactivity test was prepared in laboratory using analytical grade chemicals.

2.2. 3D printing

The samples of PLA and metal/metal alloy filled PLA nanocomposites were fabricated by the FFF AM using a commercial 3D printer, Fig. 1A (Creator Pro 3D printer, Flashforge Corporation, Zhejiang, China). The filament of 1.75 mm diameter was used to prepare the specimens. The parameter used for the 3D printing of samples are presented in Table 2. In the fabrication process, the filaments are fed through a pinch roller feed mechanism to the heated nozzle. The filament is melted and pushed through the nozzle and the melt is deposited onto a pre-heated print bed. All the biological and compression (Fig. 1C and D) scaffolds were designed to have a relative density of 50% (Fig. 1B) with a pore diameter of ~400 µm.

Table 1
Samples ID and filler properties.

Sample	ID	Wt. % of filler	Filler morphology	Filler size
Polylactic acid	PLA	0	-	-
Copper filled PLA	PLA-Cu	~70	Spherical	~50–70 µm
Bronze filled PLA	PLA-Br	~75	Spherical	~60–100 µm
Silver filled PLA	PLA-Ag	~4	Flakes	~5 × 90 µm

Surface modification: The surfaces of the 3D printed samples were modified by exposing them to acetic acid for a short duration (5 min) followed by rinsing with distilled water. Etching action of acetic acid introduces, a thin porous (few microns) network on the surfaces of PLA (Fig. 1E treated SEM image). The process of surface modification is briefly described in Fig. 1E. As shown in the schematic and the corresponding SEM images, the metal particles are exposed after the treatment and a porous network is created.

2.3. Characterization of filaments and fabricated samples

Thermal characterization: Thermal characterization of the filaments is performed to find out the glass transition temperature (T_g) and the melting temperature (T_m). Differential scanning calorimetry (DSC) was performed on a DSC 404, F1 (NETZSCH high temperature DSC) instrument under a nitrogen flux of 20 ml/min. The samples of ~10 mg were subjected to a heating scan of 30–250 °C, at a rate of 10 °C/min. Thermogravimetric analysis (TGA) was performed on a STA 449 F3 (NETZSCH) instrument in the temperature range of 25–600 °C under a flux of 20 ml/min in nitrogen environment in order to quantify the fraction of metal/metal alloy particles present in PLA matrix in the form of solid residue in the filament.

Microstructures of 3D printed samples: The microstructures and surface morphologies of the 3D-printed samples were observed using scanning electron microscopy (The FEI Nova NanoSEM 650) with an accelerating voltage of 5 kV and a spot size of 2.5 µm. A thin layer of Au/Pt (~10 nm) was deposited on the surface, using sputter coater, to make it conductive before observing in SEM. To observe the internal morphology, the printed samples were cryogenically fractured followed by sputter coating and used for SEM imaging.

Phase characterization: The phases present in the filaments and 3D printed samples were characterized by X-Ray diffraction (XRD) to confirm the presence of filler in the filaments. XRD analysis was also performed on the bioactivity tested sample's surfaces to confirm the presence of apatite layer on the surface of samples. Cu_α radiation ($\lambda = 1.541 \text{ \AA}$) operated at 40 kV and 30 mA was used as X-ray source (using XRD PAN analytical Empyrean diffractometer) with a scan speed of 2.4°/min, step size of 0.02° with 2θ ranging from 20° to 60°.

Surface wettability: The surface wettability of the samples were measured using contact angle Goniometer (Krüss GmbH Drop Shape Analyzer, DSA, Germany) by putting a drop of 10 µL of deionized water (DI) water on the surfaces of the samples through a needle. Sessile drop method in the static mode was utilized to make the drop and tangent method is used to measure the surface wettability. On each sample, at least 3 droplets were formed at three different locations and the average of all nine values were reported.

Mechanical Properties: Tensile properties of the 3D printed dogbone samples (100% relative density) were measured using universal testing machine (UTM) (Zwick-Roell 2005) at a constant crosshead speed of 5 mm/min at ambient temperature with a load cell of 2.5 kN as per ASTM D638 standard. The Modulus, tensile strength and elongation were calculated from stress-strain response obtained from tensile tests. The stiffness of the 3D printed scaffolds (50% relative density) were evaluated from compression tests, according to ASTM D-695 standard. The compression tests were performed using a UTM (Instron 5960, USA) equipped with 50 kN load cell. The stiffness of the scaffolds was calculated as the slope of the initial portion of the stress-strain curve.

Water absorption capacity: The water absorption capacity of the 3D printed scaffolds was tested following the method reported by ASTM standard D570 (ASTM D570-98(2018), 2018). The scaffolds were immersed in distilled water for 24 h, at room temperature. After the immersion time, samples were removed from water and weighed. Dry weight of the samples was also recorded before immersion in water. The water absorption capacity was calculated using following equation (Ramadass et al., 2014):

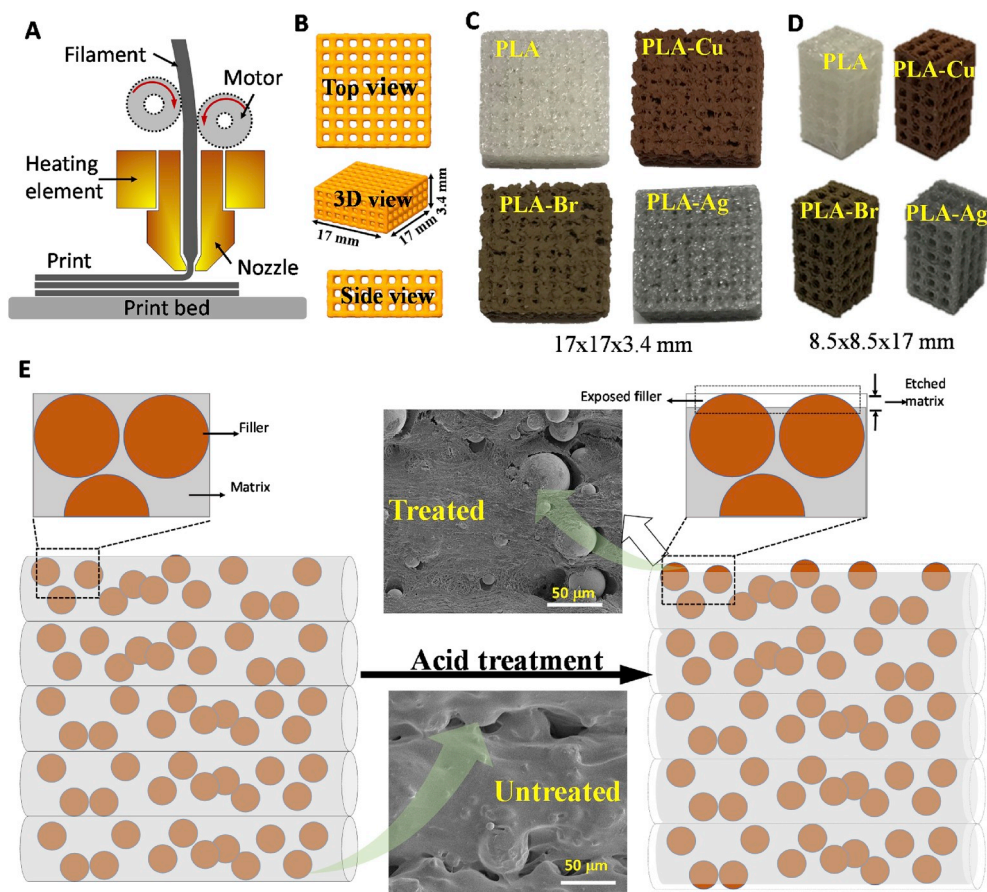


Fig. 1. (A) Schematic of the FFF 3D printing, (B) CAD model of the scaffold, (C) 3D printed scaffolds for bioactivity and antibacterial study, (D) 3D printed scaffolds for compression test and (E) Surface modifications via acid treatment of the 3D printed scaffolds.

Table 2

Process parameters for FFF AM.

Parameters	Parameters
Speed of nozzle movement	1800 mm/min; first layer 300 mm/min
Nozzle temperature	230 °C
Bed temperature	60 °C
Layer height	0.1–0.3 mm
Extrusion width	0.48 mm
Infill density	100% for all the specimens

$$\text{Water absorption capacity (\%)} = \frac{W_s - W_d}{W_d} \times 100$$

Where W_s is the soaked weight and W_d is the dry weight of the scaffolds.

2.4. Biological characterization of the samples

Bioactivity: *In-vitro* bioactivity test on triplicate of all samples was conducted by immersing them in the SBF (Alam et al., 2015). Samples were immersed in SBF for 72 h in an incubator at 37 °C and then dried in an oven overnight and examined under SEM to observe the growth of apatite layer on the surface of the samples. These grown apatite layers were further characterized by XRD to further confirm the apatite layers.

Bacterial viability assay: All the samples were tested for antibacterial performance against gram-negative *E. coli* (ATCC #25922) and gram positive *S. aureus* (ATCC #25923) respectively. The samples were ultrasonicated for 25 min followed by 45 min of autoclaving. After that, they were sterilized under ultraviolet (UV) light for 30 min. The samples were then immersed in ethanol for 60 min and then in

phosphate-buffered saline (PBS) for 15 min. All the samples were seeded with 100 μ l of 0.1 optical density (OD) bacteria solution. 700 μ l of fresh Luria broth (LB) solution was added to each sample and the samples were then incubated for 4 h at 37.4 ± 0.5 °C. Samples were then removed from the incubator and MTT [3(4,5-dimethylthiazol-2-yl)-2,5-diphenyl tetrazolium bromide]] was added to them facilitating the formation of formazan crystals which are then treated with 200 μ l DMSO (dimethyl sulfoxide) to form a purple solution. The extent of bacterial growth in the samples is estimated by evaluating the absorbance (OD) of these purple solutions via UV–vis spectrophotometer at 600 nm wavelength. PLA sample is taken as the control, as no additive is incorporated in it that can restrict the growth of bacteria in this sample and the percentage change in absorbance relative to PLA was reported.

3. Results and discussion

3.1. Physicochemical characterization

The results obtained from DSC analysis in order to evaluate the glass transition temperature (T_g) and melting temperature (T_m) are shown in Fig. 2. A comparison between the DSC thermograms of neat PLA and metal/alloy filled PLA is reported in Fig. 2a. The results of DSC indicate that the presence of fillers in PLA reduces T_m and T_g substantially from 171 °C to 151 °C and from 125 °C to 100 °C respectively (for more details, please refer Table 3).

The thermograms obtained from the TGA profile evidenced a solid residue of filler materials in the filaments as shown in Fig. 2b. PLA-Cu, PLA-Br and PLA-Ag showed about 70%, 75% and 4% of solid residue respectively, whereas no solid residue was seen for neat PLA. Furthermore the thermograms of PLA and metal/alloy filled PLA filaments

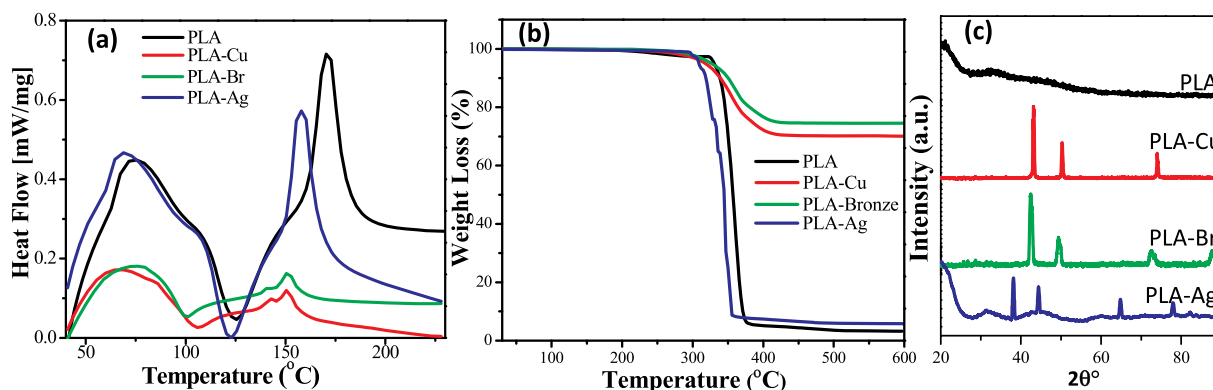


Fig. 2. (a) DSC thermograms of filaments of each samples, (b) Weight loss (%) with respect to temperature obtained from TGA analysis and (c) XRD spectra of the 3D printed samples showing the presence of fillers in the PLA matrix.

Table 3
Thermal properties of the filaments.

Sample	Wt. % of filler	T _m (°C)	T _g (°C)
PLA	0	171.0	125.5
PLA-Cu	~70	151.5	103.9
PLA-Br	~75	151.3	100.4
PLA-Ag	~4	157.0	122.6

indicate that the presence of metal/alloy fillers do not influence the degradation temperature.

Fig. 2c shows the XRD spectra of the 3D printed samples where it is clear that the neat PLA is amorphous in nature as indicated by the existence of only a broad hump in the XRD pattern. However crystalline peaks were observed in metal/metal alloy filled PLA samples. The hump from the XRD pattern of the PLA-Cu and PLA-Br is not visible because higher intensity of metal/alloy particles (copper and bronze) suppressed the intensity of the hump. The small humps are still visible in PLA-Ag because of lower weight fraction (~4%) of silver content.

The microstructural analysis of the 3D printed samples was performed under SEM and the micrographs are shown in Fig. 3. The top surface of the samples was observed to see the print layers and surface morphology. A smooth surface of neat PLA observed is shown in Fig. 3a. The beads of the metal/alloy filled PLA samples showed the presence of wrinkled surface as compared to neat PLA. The presence of filler particles is clearly visible from top surface (Fig. 3b and c; left side) on the

surface of the composite samples. The samples were further fractured cryogenically to observe the internal morphology of the printed structure. The presence of spherical (size ~ 70–100 μm) particles were observed in PLA-Cu and PLA-Br samples (Fig. 3b and c; right side) whereas flakes were observed in PLA-Ag sample (Fig. 3d; right side).

The static water contact angle (WCA) on the surface of scaffolds was also measured and the representative digital images of the droplets are shown in the inset of microstructure of each sample. The wettability of composite samples decreases due to the presence of copper and bronze particles and contact angle increases from ~59.3° (neat PLA) to 111.1° and 103.7° for PLA-Cu and PLA-Br respectively. However no significant change in the wettability of composite samples was observed with silver reinforcement (WCA of ~53.4°). Fig. 4 shows the results of water absorption capacity of 3D printed scaffolds. The water absorption capacity was quantified by immersing the samples in distilled water for different time periods. The water absorption capacity was maximum for neat PLA (89%) followed by PLA-Ag scaffold (64%), whereas PLA-Cu and PLA-Br showed lower absorption capacity of about 36% and 30% respectively. The lower water absorption capacity of PLA-Cu and PLA-Br scaffolds can be related to their lower wettability.

The decrease in the water absorption capacity of PLA-Ag composite scaffold is probably due the presence of porous and rough struts, caused by presence of flake-like silver particles.

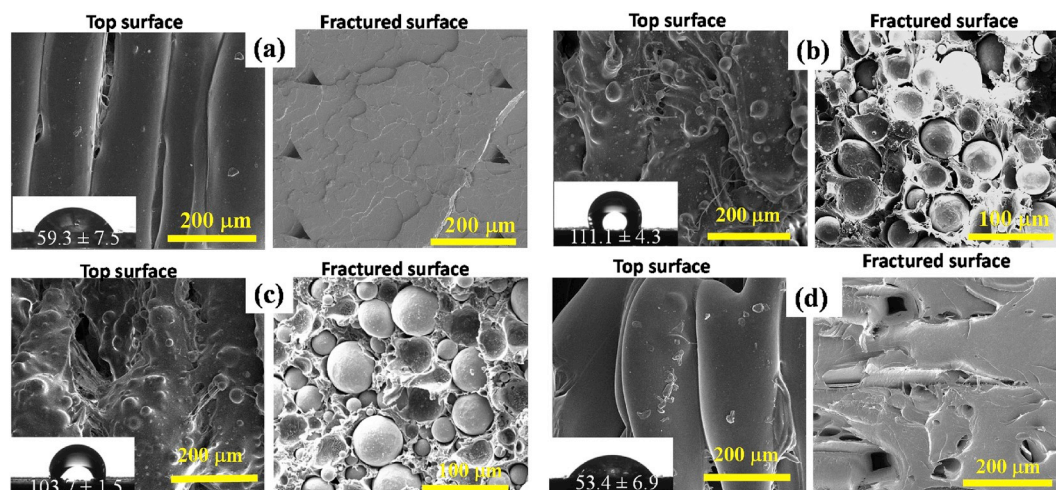


Fig. 3. SEM micrographs of the 3D printed sample surfaces. (a) PLA, (b) PLA-Cu, (c) PLA-Br and (d) PLA-Ag. Micrographs were taken from the top of the printed scaffold (left) and cryogenically fractured surfaces (right) for each sample. The static water contact angles are presented in the inset of SEM micrographs of each sample.

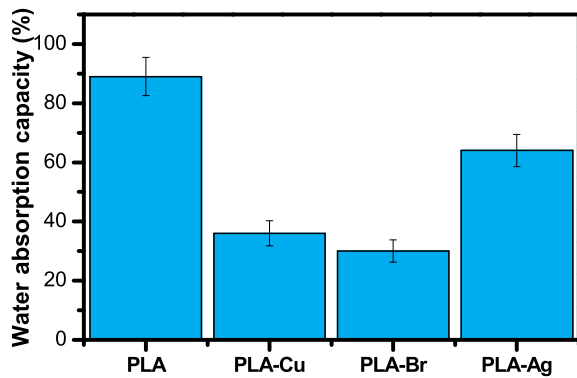


Fig. 4. Water absorption capacity of 3D printed scaffolds observed after immersion in water for 24 h.

3.2. Mechanical properties

The representative stress-strain curves obtained from the tests are shown in Fig. 5a and b and the measured results are summarized in Table 4. The maximum stress observed on the samples was reported and tensile toughness was determined from the area under the curve, reflecting the amount of work done up to the fracture of the sample.

Both the elastic modulus and elongation at break increased due to reinforcement of metals/metallic alloy particles into PLA matrix (see Table 4). The elastic modulus for neat 0°PLA was 1.54 GPa and it increased to 1.65, 1.70 and 1.59 GPa for PLA-Cu, PLA-Br and PLA-Ag samples respectively. The elastic modulus of the all the samples decreased when printed in 90° orientation. The elastic modulus for neat PLA decreased from 1.54 GPa (0°) to 1.26 GPa (90°). Tensile strength of PLA-Cu and PLA-Br samples decreased drastically however PLA-Ag

showed an increase in the tensile strength for 90° print orientation. Among all samples PLA-Ag showed the superior tensile properties.

The compression test on the 3D printed scaffolds was performed and the representative stress-strain plot is shown in Fig. 5c. Three stages were observed, i.e. an initial linear elastic region followed by a plateau of almost constant stress but increasing strain which is then terminated by an exponential increase in the stress (densification). From the compression test results, the stiffness is calculated as the slope of the initial linear part of the stress-strain curve and the values are presented in Table 4. With the reinforcement of metal particles, the stiffness of the composites increased (+103%) from 231 MPa (neat PLA) to 471 MPa (PLA-Ag).

The fractured surface of the tensile tested samples were observed under SEM and the results are shown in Fig. 6.

3.3. Bioactivation of scaffold surfaces

The surface of the 3D printed samples was treated with the acetic acid and analyzed under SEM. The micrographs obtained from SEM before and after treatment are shown in Fig. 7. PLA is covered on the surfaces of untreated samples. However acid treatment makes the surface porous and exposes filler particles as shown in Fig. 7. This thin layer of PLA becomes porous and filler particles are exposed as shown in Fig. 7b, c and d. Particles are encircled on “treated” image. Depending upon the duration of acid treatment exposed surface area of the fillers can be tuned. The exposed filler particles are expected to influence antibacterial activity than those covered with PLA. The magnified images of the porous network on the surfaces of the treated samples are shown in inset of the images labeled ‘Treated’ for all the samples.

After *in vitro* bioactivity (immersion test), surfaces were observed under SEM and the micrographs obtained are shown in Fig. 8. A mineralized apatite growth on the surfaces are clearly visible on all the

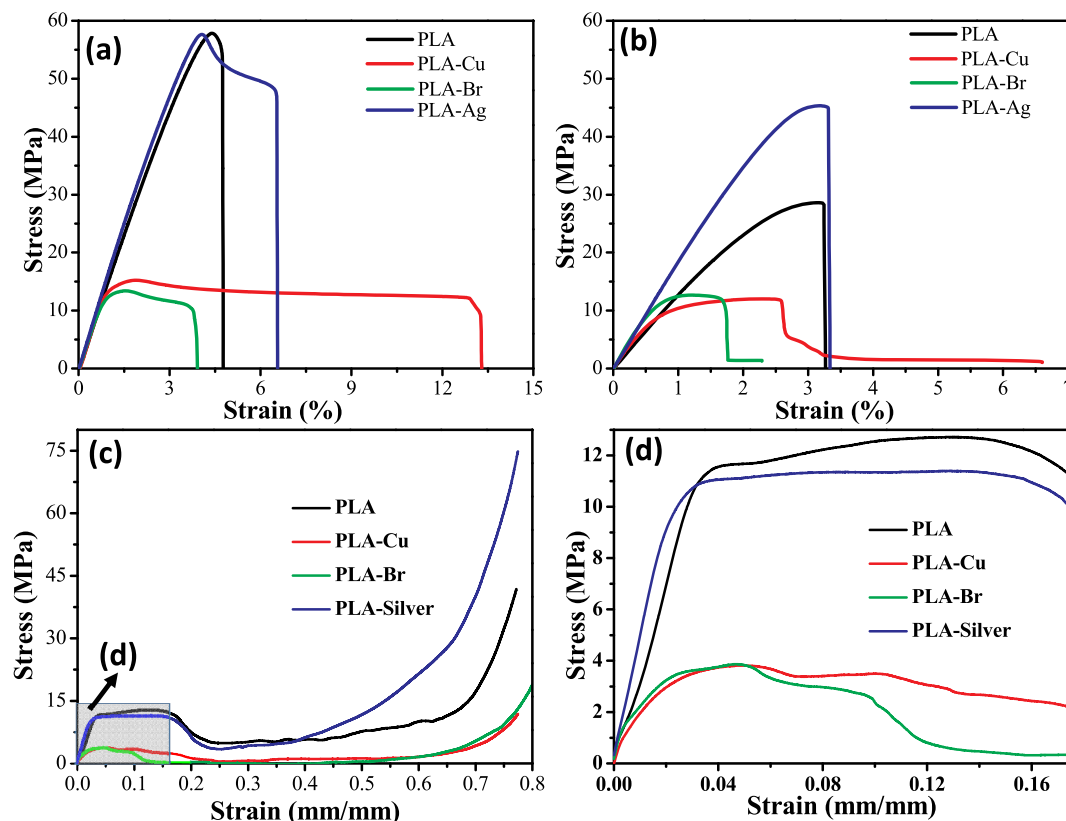


Fig. 5. Representative stress-strain curves of the samples (a) tensile test on the dogbone samples with 0° printing orientation (b) tensile test on the dogbone samples with 90° print orientation, (c) compression test of the scaffold and (d) magnified compression stress-strain plot shown in figure (c).

Table 4

Mechanical properties of PLA and is nanocomposite samples obtained from tensile and compression tests. The values in the brackets are % change with respect to neat PLA.

Properties	Printing direction	PLA	PLA-Cu	PLA-Br	PLA-Ag
Young's modulus (GPa)	0°	1.54 ± 0.06	1.65 ± 0.08 (7.7)	1.70 ± 0.12 (10.3)	1.59 ± 0.14 (3.2)
	90°	1.26 ± 0.04	1.32 ± 0.08 (4.7)	1.61 ± 0.12 (27.7)	1.43 ± 0.09 (13.4)
Tensile strength (MPa)	0°	57.49 ± 1.8	15.22 ± 1.1 (-73.5)	13.62 ± 1.3 (-76.3)	55.69 ± 2.2 (-3.1)
	90°	28.59 ± 2.2	10.01 ± 1.8 (-64.9)	10.54 ± 1.6 (-63.1)	37.77 ± 2.3 (32.1)
Toughness (J/m ³)	0°	160.23 ± 5.4	168.4 ± 6.3 (4.8)	40.97 ± 1.7 (-74.4)	295.75 ± 11.4 (84.5)
	90°	57.49 ± 3.2	27.41 ± 2.7 (-52.3)	14.90 ± 1.1 (-74.0)	75.73 ± 2.6 (31.7)
Elongation at break (%)	0°	4.7 ± 0.6	15.22 ± 0.9 (223.8)	13.62 ± 1.2 (189.7)	6.3 ± 0.7 (34.0)
	90°	3.14 ± 0.6	2.33 ± 0.08 (-25.7)	1.21 ± 0.08 (-61.4)	3.17 ± 0.12 (0.97)
Stiffness (MPa)	Scaffold	231.74 ± 5.4	316.86 ± 9.7 (36.7)	383.68 ± 7.4 (65.5)	471.69 ± 12.1 (103.5)

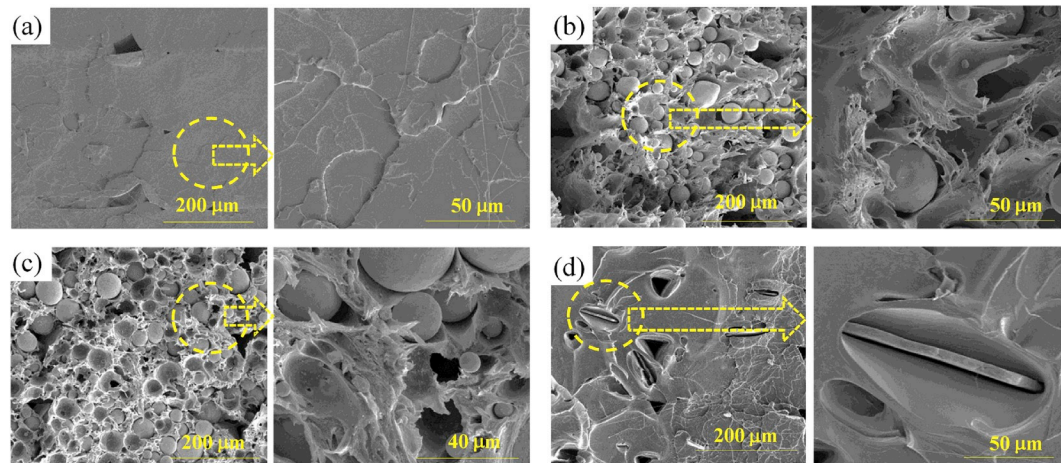


Fig. 6. The micrographs of the fractured surfaces of after the tensile test (a) PLA, (b) PLA-Cu, (c) PLA-Br and (d) PLA-Ag. The magnified images of the circled portion is shown as right side of the micrograph for each sample.

samples. Apatite growth on neat PLA sample surface, before and after surface treatment is shown in Fig. 8a. The growth of apatite on the treated samples is interestingly increased and the morphology of the apatite resembles fully grown mushroom as shown in Fig. 8b and c (from the morphologies (dendrimers and spherulite) observed on non-treated surfaces). The mineralization of the apatite crystals depends on the pH of the medium, adsorption and release of ions at the interface and surface wettability. Apatite growth on PLA-Ag samples surfaces are shown in Fig. 8d. The growth of the apatite was further characterized by XRD and results are presented in Fig. 9. It was quantified by taking the ratio of the integrated area of the apatite and area of all other peaks. It is confirmed from the quantification of results via XRD that the apatite growth is increases due to surface treatment for all the samples probably due to the presence of porous network and exposure of particles. The fraction of apatite growth before and after surface treatments are compared and presented in Table 5.

3.4. Antibacterial activity

The quantitative estimation of the antibacterial properties of scaffolds was done via viability assay and the results are shown in Fig. 10.

The samples were incubated in the presence of *E. coli* (gram-negative), rod shape, as well as with *S. aureus* (gram-positive), grapes like for 4 h and then absorbance recorded to evaluate the number of live bacteria which were attached on the surface of the samples. The percentage (%) absorbance with respect to neat PLA is reported in the bar graphs of Fig. 10. It clear from the antibacterial assay (from the changes in the % OD, shown in bar graphs) that the surface treatment with acetic acid enhanced the bactericidal properties substantially with *E. coli*. However the effect of surface treatment was not dominant with the *S. aureus*. The effect of metal/alloy reinforcement has enhanced anti-bacterial activity. Among untreated samples PLA-Br followed by PLA-Ag showed the higher anti-bacterial activity. Among the surface treated samples, PLA-Cu showed highest anti-bacterial property followed by PLA-Br composite sample.

The enhancement in the anti-bacterial properties of metal/alloy filled PLA samples are due the bactericidal nature of metals/alloy. The role of metallic/metallic alloy particles in enhancing anti-bacterial properties are mainly from direct contact killing (Codipă et al., 2010; Vaidya et al., 2017). It is reported by Panaeck et al. (Panaček et al., 2006) that gram positive (*E. Coli*) is more resistant towards silver than gram negative (*S. aureus*) and we also observed a similar result in our current

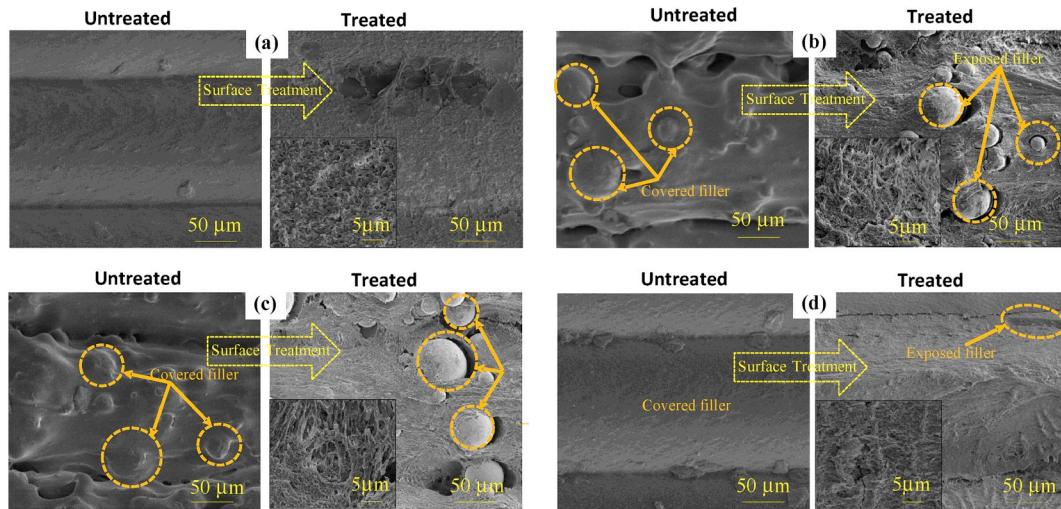


Fig. 7. SEM micrographs of the surfaces of the 3D printed samples before and after acid treatment. (a) PLA, (b) PLA-Cu, (c) PLA-Br and (d) PLA-Ag. The magnified images are shown in the inset of the treated images.

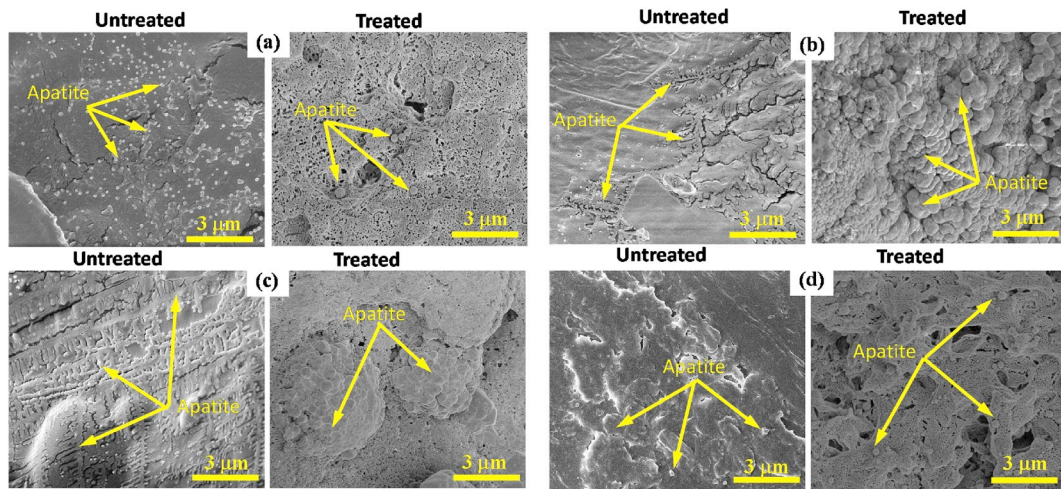


Fig. 8. SEM micrographs of the apatite grown on the surface of 3D printed samples (a) PLA (b) PLA-Cu, (c) PLA-bronze and (d) PLA-Ag. The apatite grown on treated and untreated samples are shown.

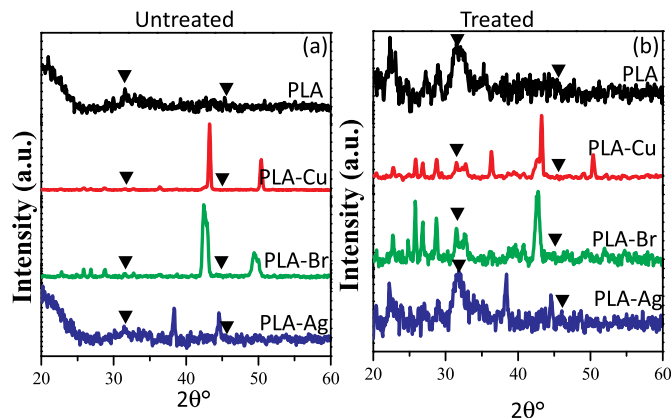


Fig. 9. XRD spectra of the apatite grown on the surface of the samples (a) untreated samples and (b) treated samples.

Table 5

Quantification of bioactivity form XRD data.

Samples	Fraction of apatite (%) (untreated samples)	Fraction of apatite (%) (acid treated samples)
PLA	8.44 ± 0.23	11.63 ± 1.07 (+37.79)
PLA-Cu	4.85 ± 0.41	9.72 ± 0.63 (+100.41)
PLA-Br	5.17 ± 0.30	6.02 ± 0.56 (+24.12)
PLA-Ag	8.16 ± 0.83	9.70 ± 0.81 (+18.87)

study. Surface treatment showed further enhancement in the anti-bacterial activity with *E.coli* which can be attributed to the exposed surface of the filler particles due to surface etching of the scaffold. However with *S. aureus*, the effect of metal/alloy reinforcement remained dominant over the effect of surface treatment. Surface treatment also created a thin porous structure on the surfaces. The thin porous surface gives rise to a rougher surface which may have helped

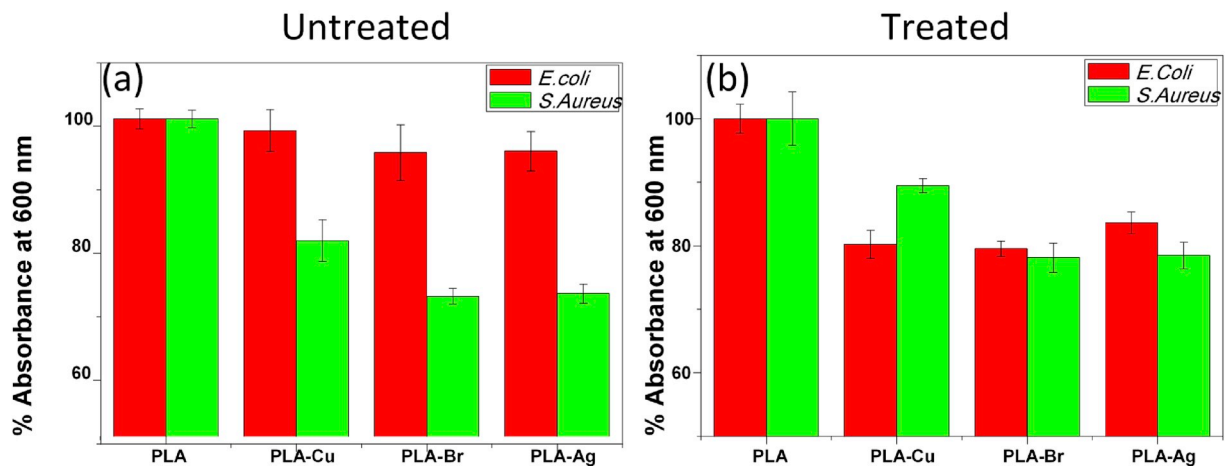


Fig. 10. Analysis of relative viability of *E. coli* and *S. aureus* showing the bactericidal property of various scaffolds (a) untreated samples and (b) treated samples compared with neat PLA.

S. aureus to increase the viability to some extent as found in our previous work (Alam and Balani, 2017; Alam et al., 2019b). Overall both, filler reinforcement and surface treatment enhanced the antibacterial activity of the metal/alloy filled PLA composites.

4. Conclusions

Anti-bacterial scaffolds, of PLA and metallic/metallic alloy particles filled PLA, were prepared via FFF AM with copper, bronze and silver particles. Thermal properties obtained from DSC showed decrease (5–10 °C) in T_m and T_g of the composites but they did not have any effect on the printability of the scaffolds. The addition of metallic/metallic alloy particles into the PLA increases the elastic modulus (~3–10% for 0° orientation) and elongation (up to 200%) but decreases the tensile strength. PLA as well as nanocomposite PLA samples printed in 90° orientation showed poor mechanical properties as compared to the samples printed in 0° orientation. The surface of scaffolds were further modified with acetic acid to create a thin micro-porous network. The wettability of PLA composites decreased from ~59° to ~100° due to the presence of filler particles and rougher surface of the printed structure as compared to neat PLA. Metal/alloy filled PLA showed antibacterial activity with gram-positive (~10% less viability) as well as with gram-negative (~30% less viability) bacterial cells. Anti-bacterial properties due to surface treatment were enhanced with *E. coli* (up to 18% less viability), whereas with *S. Aureus*, the surface treatment doesn't show any effect. Among all samples, PLA-Ag showed superior mechanical and anti-bacterial properties. The results indicate that metal/alloy filled PLA nanocomposite could be a potential candidate for bone scaffold applications.

Declaration of competing interest

All authors have participated in (a) conception and design, or analysis and interpretation of the data; (b) drafting the article or revising it critically for important intellectual content; and (c) approval of the final version.

Acknowledgement

This publication is based upon work supported by the Khalifa University of Science and Technology under Award No. CIRA-2018-128. Authors would like to thank Prof. Kantesh Balani, MSE, IIT Kanpur, for his constructive comments on the manuscript.

Appendix A. Supplementary data

Supplementary data to this article can be found online at <https://doi.org/10.1016/j.jmbbm.2019.103576>.

References

- Alam, F., Balani, K., 2017. Adhesion force of staphylococcus aureus on various biomaterial surfaces. *J. Mech. Behav. Biomed. Mater.* 65, 872–880.
- Alam, F., Kumar, A., Patel, A.K., Sharma, R.K., Balani, K., 2015. Processing, characterization and fretting wear of zinc oxide and silver nanoparticles reinforced ultra high molecular weight polyethylene biopolymer nanocomposite. *J. Occup. Med.* 67, 688–701.
- Alam, F., Choosri, M., Gupta, T.K., Varadarajan, K.M., Choi, D., Kumar, S., 2019a. Electrical, mechanical and thermal properties of graphene nanoplatelets reinforced UHMWPE nanocomposites. *Mater. Sci. Eng., B* 241, 82–91.
- Alam, F., Kumar, S., Varadarajan, K.M., 2019b. Quantification of adhesion force of bacteria on the surface of biomaterials: techniques and assays. *ACS Biomater. Sci. Eng.* 5, 2093–2110.
- Almeida, C.R., Serra, T., Oliveira, M.I., Planell, J.A., Barbosa, M.A., Navarro, M., 2014. Impact of 3-D printed PLA- and chitosan-based scaffolds on human monocyte/macrophage responses: unraveling the effect of 3-D structures on inflammation. *Acta Biomater.* 10, 613–622.
- Arif, M.F., Kumar, S., Varadarajan, K.M., Cantwell, W.J., 2018. Performance of biocompatible PEEK processed by fused deposition additive manufacturing. *Mater. Des.* 146, 249–259.
- ASTM D570-98(2018), 2018. Standard Test Method for Water Absorption of Plastics. ASTM International, West Conshohocken, PA, p. 2018. www.astm.org.
- Balogangadharan, K., Dhivya, S., Selvamurugan, N., 2017. Chitosan based nanofibers in bone tissue engineering. *Int. J. Biol. Macromol.* 104, 1372–1382.
- Bayer, I.S., 2017. Thermomechanical properties of polylactic acid-graphene composites: a state-of-the-art review for biomedical applications. *Materials* 10, 748.
- Cataldi, P., Athanassiou, A., Bayer, I., 2018. Graphene nanoplatelets-based advanced materials and recent progress in sustainable applications. *Appl. Sci.* 8, 1438.
- Cavasin, M., Giannis, S., Salvo, M., Casalegno, V., Sangermano, M., 2018. Mechanical and thermal characterization of an epoxy foam as thermal layer insulation for a glass fiber reinforced polymer. *J. Appl. Polym. Sci.* 135, 46864.
- Codipă, I., Caplan, D.M., Drăgulescu, E.-C., Lixandru, B.A.-E., Coldea, I.L., Dragomirescu, C.C., Surdu-Bob, C., Bădulescu, M., 2010. Antimicrobial activity of copper and silver nanofilms on nosocomial bacterial species. *Roman. Archiv.* 18, 204.
- Dhivya, S., Saravanan, S., Sastry, T.P., Selvamurugan, N., 2015. Nanohydroxyapatite-reinforced chitosan composite hydrogel for bone tissue repair in vitro and in vivo. *J. Nanobiotechnol.* 13, 40.
- Dong, L., Wang, S.-J., Zhao, X.-R., Zhu, Y.-F., Yu, J.-K., 2017. 3D-printed poly(ϵ -caprolactone) scaffold integrated with cell-laden chitosan hydrogels for bone tissue engineering. *Sci. Rep.* 7, 13412.
- Dugbenoo, E., Arif, M.F., Wardle, B.L., Kumar, S., 2018. Enhanced bonding via additive manufacturing-enabled surface tailoring of 3D printed continuous-fiber composites. *Adv. Eng. Mater.* 20, 1800691.
- Ertane, E.G., Dörner-Reisel, A., Baran, O., Welzel, T., Matner, V., Svoboda, S., 2018. Processing and wear behaviour of 3D printed PLA reinforced with biogenic carbon. *Adv. Tribol.* 2018.
- Feng, J., Yang, G., Zhang, S., Liu, Q., Jafari, S.M., McClements, D.J., 2018. Fabrication and characterization of β -cypermethrin-loaded PLA microcapsules prepared by emulsion-solvent evaporation: loading and release properties. *Environ. Sci. Pollut. Control Ser.* 25, 13525–13535.

- Gnanasekaran, K., Heijmans, T., Van Bennekom, S., Woldhuis, H., Wijnia, S., de With, G., Friedrich, H., 2017. 3D printing of CNT-and graphene-based conductive polymer nanocomposites by fused deposition modeling. *Appl. Mater. Today* 9, 21–28.
- Gupta, T.K., Kumar, S., Khan, A.Z., Varadarajan, K.M., Cantwell, W.J., 2018. Self-sensing performance of MWCNT-low density polyethylene nanocomposites. *Mater. Res. Express* 5, 015703.
- Harris, A.M., Lee, E.C., 2008. Improving mechanical performance of injection molded PLA by controlling crystallinity. *J. Appl. Polym. Sci.* 107, 2246–2255.
- Huang, B., Caetano, G., Vyas, C., Blaker, J.J., Diver, C., Bártolo, P., 2018. Polymer-ceramic composite scaffolds: the effect of hydroxyapatite and β -tri-calcium phosphate. *Materials* 11, 129.
- Jammalamadaka, U., Tappa, K., 2018. Recent advances in biomaterials for 3D printing and tissue engineering. *J. Funct. Biomater.* 9, 22.
- Kumar, S., Wardle, B.L., Arif, M.F., 2016. Strength and performance enhancement of bonded joints by spatial tailoring of adhesive compliance via 3D printing. *ACS Appl. Mater. Interfaces* 9, 884–891.
- Kumar, S., Gupta, T.K., Varadarajan, K.M., 2019. Strong, stretchable and ultrasensitive MWCNT/TPU nanocomposites for piezoresistive strain sensing. *Compos. B Eng.* 177, 107285.
- Levengood, S.K.L., Zhang, M., 2014. Chitosan-based scaffolds for bone tissue engineering. *J. Mater. Chem. B* 2, 3161–3184.
- Li, Q.-h., Zhou, Q.-h., Deng, D., Yu, Q.-z., Gu, L., Gong, K.-d., Xu, K.-h., 2013. Enhanced thermal and electrical properties of poly (D,L-lactide)/multi-walled carbon nanotubes composites by in-situ polymerization. *Trans. Nonferrous Metals Soc. China* 23, 1421–1427.
- Li, X., Ni, Z., Bai, S., Lou, B., 2018. Preparation and mechanical properties of fiber reinforced PLA for 3D printing materials. In: *IOP Conference Series: Materials Science and Engineering*. IOP Publishing, 022012.
- Ligon, S.C., Liska, R., Stampfl, J., Gurr, M., Mühlaupt, R., 2017. Polymers for 3D printing and customized additive manufacturing. *Chem. Rev.* 117, 10212–10290.
- Menon, A.H., Soundarya, S.P., Sanjay, V., Chandran, S.V., Balagangadharan, K., Selvamurugan, N., 2018. Sustained release of chrysin from chitosan-based scaffolds promotes mesenchymal stem cell proliferation and osteoblast differentiation. *Carbohydr. Polym.* 195, 356–367.
- Nakagaito, A.N., Fujimura, A., Sakai, T., Hama, Y., Yano, H., 2009. Production of microfibrillated cellulose (MFC)-reinforced polylactic acid (PLA) nanocomposites from sheets obtained by a papermaking-like process. *Compos. Sci. Technol.* 69, 1293–1297.
- Panáček, A., Kvítek, L., Prucek, R., Kolář, M., Večeřová, R., Pizúrová, N., Sharma, V.K., Nevečná, T., Zbořil, R., 2006. Silver colloid nanoparticles: synthesis, characterization, and their antibacterial activity. *J. Phys. Chem. B* 110, 16248–16253.
- Paolini, A., Leoni, L., Giannicchi, I., Abbaszadeh, Z., D'Oria, V., Mura, F., Dalla Cort, A., Masotti, A., 2018. MicroRNAs delivery into human cells grown on 3D-printed PLA scaffolds coated with a novel fluorescent PAMAM dendrimer for biomedical applications. *Sci. Rep.* 8, 13888.
- Patole, S.P., Reddy, S.K., Schiffer, A., Askar, K., Prusty, B.G., Kumar, S., 2019. Piezoresistive and mechanical characteristics of graphene foam nanocomposites. *ACS Appl. Nano Mater.* 2, 1402–1411.
- Persson, M., Lorite, G.S., Kokkonen, H.E., Cho, S.-W., Lehenkari, P.P., Skrifvars, M., Tuukkanen, J., 2014. Effect of bioactive extruded PLA/HA composite films on focal adhesion formation of preosteoblastic cells. *Colloids Surfaces B Biointerfaces* 121, 409–416.
- Preethi Soundarya, S., Haritha Menon, A., Viji Chandran, S., Selvamurugan, N., 2018. Bone tissue engineering: scaffold preparation using chitosan and other biomaterials with different design and fabrication techniques. *Int. J. Biol. Macromol.* 119, 1228–1239.
- Rajkumar, A.R., Shanmugam, K., 2018. Additive manufacturing-enabled shape transformations via FFF 4D printing. *J. Mater. Res.* 33, 4362–4376.
- Ramadass, S.K., Perumal, S., Gopinath, A., Nisal, A., Subramanian, S., Madhan, B., 2014. Sol-gel assisted fabrication of collagen hydrolysate composite scaffold: a novel therapeutic alternative to the traditional collagen scaffold. *ACS Appl. Mater. Interfaces* 6, 15015–15025.
- Reddy, S., Xu, X., Guo, T., Zhu, R., He, L., Ramakrishna, S., 2018. Allotropic carbon (graphene oxide and reduced graphene oxide) based biomaterials for neural regeneration. *Curr. Opin. Biomed. Eng.* 6, 120–129.
- Saito, N., Okada, T., Horiuchi, H., Murakami, N., Takahashi, J., Nawata, M., Ota, H., Nozaki, K., Takaoka, K., 2001. A biodegradable polymer as a cytokine delivery system for inducing bone formation. *Nat. Biotechnol.* 19, 332.
- Salentijn, G.I., Oomen, P.E., Grajewski, M., Verpoorte, E., 2017. Fused deposition modeling 3D printing for (bio) analytical device fabrication: procedures, materials, and applications. *Anal. Chem.* 89, 7053–7061.
- Saravanan, S., Chawla, A., Vairamani, M., Sastry, T.P., Subramanian, K.S., Selvamurugan, N., 2017. Scaffolds containing chitosan, gelatin and graphene oxide for bone tissue regeneration in vitro and in vivo. *Int. J. Biol. Macromol.* 104, 1975–1985.
- Sharif, S., Ai, J., Azami, M., Verdi, J., Atlasi, M.A., Shirian, S., Samadikuchaksaraei, A., 2018. Collagen-coated nano-electrospun PCL seeded with human endometrial stem cells for skin tissue engineering applications. *J. Biomed. Mater. Res. B Appl. Biomater.* 106, 1578–1586.
- Shirai, M.A., Zanela, J., Kunita, M.H., Pereira, G.M., Rubira, A.F., Müller, C.M.O., Grossmann, M.V.E., Yamashita, F., 2018. Influence of carboxylic acids on poly (lactic acid)/thermoplastic starch biodegradable sheets produced by calendering–extrusion. *Adv. Polym. Technol.* 37, 332–338.
- Singh, R., Sharma, R., Ranjan, N., 2014. Four-Dimensional Printing for Clinical Dentistry. *Sivashankari, P.R., Prabakaran, M., 2016. Prospects of chitosan-based scaffolds for growth factor release in tissue engineering. Int. J. Biol. Macromol.* 93, 1382–1389.
- Sousa, S., Costa, A., Silva, A., Simões, R., 2019. Poly (lactic acid)/cellulose films produced from composite spheres prepared by emulsion-solvent evaporation method. *Polymers* 11, 66.
- Tanodekaew, S., Channasanon, S., Kaewkong, P., Uppanan, P., 2013. PLA-HA scaffolds: preparation and bioactivity. *Procedia Eng.* 59, 144–149.
- Ubaid, J., Wardle, B.L., Kumar, S., 2018. Strength and performance enhancement of multilayers by spatial tailoring of adherend compliance and morphology via multimaterial jetting additive manufacturing. *Sci. Rep.* 8, 13592.
- Upadhyay, K., Dwivedi, R., Singh, A.K., 2017. Determination and Comparison of the Anisotropic Strengths of Fused Deposition Modeling P400 ABS, *Advances in 3D Printing & Additive Manufacturing Technologies*. Springer, pp. 9–28.
- Vaidya, M.Y., McBain, A.J., Butler, J.A., Banks, C.E., Whitehead, K.A., 2017. Antimicrobial efficacy and synergy of metal ions against *Enterococcus faecium*, *Klebsiella pneumoniae* and *acinetobacter baumannii* in planktonic and biofilm phenotypes. *Sci. Rep.* 7, 5911.
- Volpe, V., De Filitto, M., Klofacova, V., De Santis, F., Pantani, R., 2018. Effect of mold opening on the properties of PLA samples obtained by foam injection molding. *Polym. Eng. Sci.* 58, 475–484.
- Wang, X., Jiang, M., Zhou, Z., Gou, J., Hui, D., 2017a. 3D printing of polymer matrix composites: a review and prospective. *Compos. B Eng.* 110, 442–458.
- Wang, X., Li, G., Liu, Y., Yu, W., Sun, Q., 2017b. Biocompatibility of biological material polylactic acid with stem cells from human exfoliated deciduous teeth. *Biomed. Rep.* 6, 519–524.
- Xiaoyong, S., Liangcheng, C., Honglin, M., Peng, G., Zhanwei, B., Cheng, L., 2017. Experimental analysis of high temperature PEEK materials on 3D printing test, *Measuring Technology and Mechatronics Automation (ICMTMA)*. In: 2017 9th International Conference on. IEEE, pp. 13–16.
- Xu, B., Dou, H., Tao, K., Sun, K., Ding, J., Shi, W., Guo, X., Li, J., Zhang, D., Sun, K., 2011. “Two-in-One” fabrication of Fe₃O₄/MePEG-PLA composite nanocapsules as a potential ultrasonic/MRI dual contrast agent. *Langmuir* 27, 12134–12142.